PHYSICAL REVIEW MATERIALS **4**, 013606 (2020)

Editors' Suggestion

First-principles investigation of the phase stability and early stages of precipitation in Mg-Sn alloys

Kang Wang, Du Cheng, Chu-Liang Fu, and Bi-Cheng Zhou[*]
Department of Materials Science and Engineering, University of Virginia, Charlottesville, Virginia 22904, USA

(Received 29 August 2019; published 28 January 2020)

Recently, remarkable experimental progress has been made toward understanding the metastable phases in Mg-Sn alloys, a promising candidate for rare-earth free Mg alloys. However, the detailed structures, stability, and formation mechanisms of these metastable phases at early stages of precipitation remain unclear. Here, we report a first-principles study of the ground-state and finite-temperature phase stability of hexagonal closest packed (HCP)- and face-centered cubic (FCC)-based phases in Mg-Sn alloys. The ground-state phases are searched by the cluster expansion approach coupled with energy input from first-principles calculations. The Monte Carlo simulations with Hamiltonian from the cluster expansion are performed to calculate the configurational free energies and the corresponding metastable phase diagrams are constructed. Our calculations reveal rich varieties of orderings on HCP and FCC lattices, metastable Mg_3Sn phases with $L1_2$ and $D0_{19}$ structures, and possible precursors for Guinier-Preston (G.P.) zones. Further analysis of the vibrational free energy indicates that $L1_2$ Mg_3Sn is stabilized by vibrational entropy at high temperatures. A new precipitation sequence for Mg-Sn alloys is suggested, i.e., supersaturated solid solution → G.P. zone → $D0_{19}$ Mg_3Sn → $L1_2$ Mg_3Sn → βMg_2Sn.

DOI: 10.1103/PhysRevMaterials.4.013606

I. INTRODUCTION

The increasing demand for light-weight structural materials has led to increased interest in Mg-based alloys, which, however, is limited due to inadequate mechanical properties and corrosion resistance compared with steels, Al-based, Ni-based, or Ti-based alloys [1,2]. Among various Mg alloys, Mg-Sn-based alloys, free of expensive rare-earth elements, have become promising candidates for structural applications due to high solubility of Sn in Mg (14.5 wt.% at 561 °C), precipitate hardenability by β Mg_2Sn phase, and good castability resulting from the eutectic reaction at 561 °C in Mg-Sn system [1,3,4]. In the equilibrium phase diagram, the only intermetallic phase Mg_2Sn in Mg-Sn-based alloys has a melting point of 770 °C [3,4], which is much higher than that of $Mg_{17}Al_{12}$ phase (462 °C) in Mg-Al alloys [4,5]. The presence of stable β phase is shown to improve the strength and high-temperature creep resistance via precipitation strengthening [1]. The electrochemical properties of Mg-Sn alloys are also appealing. Alloying of Sn is shown to inhibit the cathodic H_2 evolution in aqueous environment, thus improving the corrosion resistance of Mg-Sn alloys [6,7]. The nontoxic nature of Sn made Mg-Sn alloys biocompatible [8,9], thus attractive for medical applications, such as orthopedic implant [10] and bone screws [11].

Despite the merits of Mg-Sn alloys, the strengthening Mg_2Sn phase usually has a coarse distribution and lie on the basal plane of Mg matrix [12] or at the grain boundaries of as-cast Mg-Sn alloys [13], resulting in poor mechanical response since the former is not effective in impeding gliding of dislocations on basal plane [1] while the latter might be the nucleation sites for voids during fracture process [14]. Due to its equilibrium nature, it takes a long time (e.g., weeks) to reach peak hardness [15,16], making it difficult to improve the mechanical properties in industrial practice. Consequently, the search for metastable phases that has strengthening effects has come to attention. In addition to the equilibrium β phase, recent studies of the microstructures of cast, solutionized and artificially aged (100–250 °C, lower than the typical aging temperature to form β Mg_2Sn phase [1]) Mg-9.8Sn (wt.%) alloy showed the presence of Guinier-Preston (G.P.) zones and metastable coherent precipitates with $L1_2$ structure [17,18]. During heating process with 20 K/min, $D0_{19}$ type Mg_3Sn phase starts to form in Mg-1.5Sn (at.%) solid solution at 101 °C, and is found to be responsible for its increased hardness [19]. $D0_{19}$ Mg_3Sn phase is also observed in as-solidified microstructures of Mg-9.76Sn (wt.%) alloys processed by a nonequilibrium melt spinning method [20]. Despite such experimental progress, the detailed structures and stability of these metastable phases (i.e., various G.P. zones, $L1_2$ and $D0_{19}$ Mg_3Sn) and their roles in the early stages of precipitation remain unclear.

The cluster expansion (CE) method with energy input from first-principles calculations based on density functional theory (DFT) has been proven to be a powerful tool to explore the structures and stability of phases in various systems [21,22]. In the current work, CE calculations are performed for hexagonal closest packed (HCP) and face-centered cubic (FCC) Mg-Sn alloys to search for the stable / metastable phases at ground state and (semigrand) canonical lattice Monte Carlo (MC) simulations are adopted to calculate the free energies and phase diagrams. In Sec. II, the detailed methods and parameters of the DFT, CE, MC, and short-range order analysis are given. In Sec. III, the ground-state structures and stability of metastable phases from CE calculations are presented. In Sec. IV, the finite-temperature stabilities of phases from MC simulations are discussed and the corresponding phase

---

[*] bicheng.zhou@virginia.edu

diagrams are constructed. In Sec. V, the effect of lattice vibrations on the stability of $L1_2$ phase is analyzed. In Sec. VI, the nucleation of the metastable phases and precipitation sequence are discussed.

II. METHODOLOGY

A. Coarse graining of partition function

For a material at finite temperatures, the free energy usually consists of the contributions from several mechanisms, i.e., lattice structures, atomic configurations, lattice vibrations, excitations of electronic states and magnetic configurations if the material displays magnetism. In principle, the free energy can be calculated by the partition function [21,23],

$$Z = \sum_{L} \sum_{\sigma \in L} \sum_{\upsilon \in \sigma} \sum_{e \in \upsilon} \exp\left[-\frac{E(L, \sigma, \upsilon, e)}{k_B T}\right], \qquad (1)$$

where $E(L, \sigma, \upsilon, e)$ is the energy the alloy, k_B is the Boltzmann constant and T is the temperature. For a specific parent lattice L, there are three degrees of freedom that contributes to Z, i.e., the specific configuration of atoms (σ, the vector of all occupation variables $\hat{S}_i$ for each site i on a given lattice L), the vibrational state (υ, the displacement of atoms from their ideal positions), the particular electronic state (e) when ions are constrained to state σ and υ. The degrees of freedom $\{L, \sigma, \upsilon, e\}$ defines the microstate of materials on different scales and each summation defines an increasingly coarser level of hierarchy. With the partition function in Eq. (1), the free energy can, in principle, be calculated by $A = -k_B T \ln(Z)$. However, for each atomic configuration on a given lattice, calculating the total energies of so many microstates for the lattice vibrations and electronic structures is too computationally demanding. In practice, for a specific atomic configuration on a given lattice, it is often assumed that the atoms always relax to the equilibrium positions and electronic structures reduces to the electronic ground state. As such, Eq. (1) reduces to [21,23],

$$Z = \sum_{L} \sum_{\sigma \in L} \exp\left[-\frac{E^*(L, \sigma)}{k_B T}\right], \qquad (2)$$

where $E^*(L, \sigma) \equiv \min_{\upsilon,e}\{E(L, \sigma, \upsilon, e)\}$ is the energy of atomic structure of lattice L, configuration σ, and optimized atomic positions and electronic structure. For a structure with given lattice L and configuration σ, $E^*(L, \sigma)$ can be obtained by optimizing all degrees of freedom of the cell (i.e., volume, shape, and internal atomic positions) by first-principles calculations.

B. DFT and phonon calculations

First-principles calculations based on DFT were employed to calculate the ground-state structures and energies of ordering phases on HCP and FCC lattice of Mg-Sn alloys. The ion-electron interaction was described by the projector augmented plane-wave method [24] and the exchange-correlation functional was described by an improved general gradient approximation of Perdew-Burke-Ernzerhof [25], as implemented in the Vienna *ab initio* simulation package (VASP, version 5.4) [26,27]. The pseudopotentials with 8 valence electrons for Mg and 14 valence electrons for Sn were used. An energy cutoff of 520 eV was adopted for the plane-wave expansion of the electronic wave functions. The Methfessel-Paxton technique was adopted with smearing parameter of 0.2 eV for integration over k points [28]. The Brillouin zone was sampled by γ-centered grids with the k points per reciprocal atom over 10 000. For all the configurations under consideration, all degrees of freedom for the cell (e.g., volume, shape, and atomic positions) are allowed to relax for structural optimization. To improve the accuracy of energy calculations, static calculations with the tetrahedron method incorporating Blöchl correction [29] were adopted after structural relaxations. To analyze the effects of lattice vibrations on the stability of phases, the force constants matrices were calculated for several structures by the linear response method [30], which, compared with the supercell method, can better capture the splitting between longitudinal and transverse optical phonon frequencies of Mg_2Sn [31]. The supercells with 96 ($4 \times 4 \times 3$ primitive cells), 96 ($2 \times 2 \times 2$ unit cells), 96 ($2 \times 2 \times 3$ primitive cells), and 108 ($3 \times 3 \times 3$ primitive cells) atoms are used, respectively, for the force constant calculations for Mg, Mg_2Sn, $D0_{19}$, and $L1_2$ Mg_3Sn, with the k points per reciprocal atom over 6 000. Current numerical tests show that the phonon density of states (DOS) curves for $D0_{19}$ Mg_3Sn from linear response method consists of small imaginary parts, which may affect the accuracy of vibrational free energy. Hence, in the analysis, the phonon DOS for $D0_{19}$ Mg_3Sn is obtained by the supercell method. The YPHON package of Wang *et al.* [32] is adopted to extract the force constant matrix from VASP output and calculate the phonon DOS and dispersion.

C. Cluster expansion

The CE method is widely used to construct the Hamiltonian of different atomic configurations on a parent lattice due to the fact that, for a cell of N atoms for binary system, the energies of 2^N structures need to be calculated, which becomes formidable when N increases. In the CE approach, the alloy is treated using the lattice model where the lattice sites are fixed on the underlying Bravais lattice and a configuration σ is defined by specifying the occupation of each of the N lattice sites. For each configuration, one assigns a set of spin variables $\hat{S}_i$ ($i = 1, 2, \ldots, N$) to each of the N sites of the lattice, with $\hat{S}_i = 0,\ 1,\ \ldots,\ M - 1$ for M component system. As such, it is proven that the energy of a given atomic configuration on fixed lattice can be cast into [33],

$$E_{CE}(\sigma) = J_0 + \sum_{i} J_i \hat{S}_i(\sigma) + \sum_{j<i} J_{ij} \hat{S}_i(\sigma) \hat{S}_j(\sigma) + \sum_{k<j<i} J_{ijk} \hat{S}_i(\sigma) \hat{S}_j(\sigma) \hat{S}_k(\sigma) + \ldots, \qquad (3)$$

where J_0, J_i, J_{ij}, J_{ijk} are the effect cluster interactions (ECIs) for empty, point, pair, and triplet clusters. In the CE formalism, ECIs are dependent on the geometry of the corresponding clusters but independent of the atomic occupations. Once the ECIs are obtained by fitting to the energies of known structures, the energy of any configuration can be readily calculated by Eq. (3). Refer the clusters in CE as "figures" and define all symmetrically equivalent figures f belonging to class F, then Eq. (3) can be written in a compact form [34],

$$E_{\mathrm{CE}}(\sigma) = N \sum_{F} D_F J_F \bar{\Pi}_F(\sigma), \tag{4}$$

where $D_F \equiv O_F/m$ is the number of figures in class F per site, O_F is the number of figures in class F, m is the number of sites in class F, J_F is the ECI for class F, $\bar{\Pi}_F$ is the averaged correlation function for class F [34],

$$\bar{\Pi}_F(\sigma) = \frac{1}{O_F} \sum_{f} \hat{S}_1(\sigma)\hat{S}_2(\sigma)\cdots\hat{S}_m(\sigma). \tag{5}$$

With the Ising-like Hamiltonian [Eqs. (3) and (4)] for any configuration on a given lattice, the free energy can be calculated with the MC sampling method.

In the current work, the MAPS code in alloy theoretic automated toolkit (ATAT) [35–37] is adopted to generate various atomic configurations on lattice and perform the CE calculations for HCP and FCC Mg-Sn alloys. In CE, the pair, triplet, and quadruplet clusters, in addition to empty and point clusters, are adopted and the corresponding ECIs are used to fit the energy from DFT calculations. The numbers of different clusters are varied to adjust the number of fitting ECIs to minimize the leave-one-out cross validation (LOOCV) [35,36]. In this study, convergence of CE is reached once LOOCV is smaller than 5 meV/atom, no new ground state with at most 16 atoms is predicted by CE, and the ECIs do not change significantly if more structures from DFT calculations are added. All structures with up to 14 and 12 atoms are searched, respectively, to yield converged CE results for HCP and FCC, which are then adopted to search for relatively stable orderings with energy less than 5 meV/atom above the convex hull within $0 < x_{\mathrm{Sn}} < 25$ at.%. The criterion of 5 meV/atom is chosen since it is approximately the error bar for the energies predicted by converged CE. The orderings with relatively lower predicted energies are then calculated using DFT and included in the CE fitting afterward. Eventually, among the 228 and 317 structures included in the training of ECIs for HCP and FCC lattices, the largest structures have 18 and 16 atoms with the final LOOCV score being 3.5 and 3.1 meV/atom, respectively.

In CE method, it is assumed that the structures have the same symmetry of the parent lattice and atoms always sit on the ideal lattice sites, which, in general, is not the case for relaxed structures in DFT calculations. Previous calculations have shown that including the over relaxed structures will adversely affect the convergence and reliability of CE [38]. To deal with this issue, the following methods are adopted previously: (1) set a threshold value for lattice distortion [37]; (2) set a threshold value for the relaxations of atoms using normalized mean square displacements [38] or number of atoms within a shell [39]; (3) fix the shape of the lattice and only relax the volume and internal atomic positions [40]; (4) use the structure and energy at the inflection point in the relaxation path of the structures that do not resemble the underlying lattice [41]; (5) limit the range of concentrations if, outside a concentration range, the structures tend to relax away from the original lattice [37]. In the current work, two criterions are adopted to characterize the relaxation magnitude of lattice vectors and atomic positions. For the lattice vectors, the extent of relaxation without isotropic volume change or rigid rotation can be measured by the 2-norm of the distortion matrix [42],

$$d = \|(\mathbf{D} + \mathbf{D}^T)/2 - \mathbf{I}_3\|_2, \tag{6}$$

where $\mathbf{I}_3$ is the 3×3 identity matrix and $\mathbf{D}$ is the matrix required to transform the matrix of ideal lattice vectors ($\mathbf{L}_0$) to the relaxed one ($\mathbf{L}_{rlx}$) in a volume conserving manner,

$$\mathbf{D} = \left[\mathbf{L}_0/V_0^{(1/3)}\right]^{-1} \cdot \left[\mathbf{L}_{rlx}/V_{rlx}^{(1/3)}\right], \tag{7}$$

where V_0 and V_{rlx} are the volumes of the ideal and relaxed structures, respectively. This criterion for lattice distortion is implemented in ATAT [35–37]. As for the relaxations of internal atomic positions, the normalized mean square displacement (NMSD) is proposed by Nguyen *et al.* to measure the displacement of atoms from their reference positions [38],

$$\mathrm{NMSD} = \frac{1}{N V_0^{2/3}} \left[\sum_{k} \left(\mathbf{R}_k^{rlx} - \mathbf{R}_k^{0}\right)^2\right] \cdot 100\%, \tag{8}$$

where $\mathbf{R}_k^{rlx}$ and $\mathbf{R}_k^{0}$ are the Cartesian positions of kth atom in the relaxed and initial cell, respectively. The criterion of lattice distortion [d, Eq. (6)] and NMSD are adopted to examine the relaxation of structures, and for consistence, the structures with $d < 0.1$ are included in the fitting of ECIs for both HCP and FCC lattices.

D. Monte Carlo simulations

The free energies of HCP and FCC lattices as a function of composition and temperature are calculated using MC simulations with the input Hamiltonian from converged CE. The configurational space is sampled using semigrand canonical MC, where the chemical potential, volume, temperature and total number of lattice sites are fixed while the number of atoms of each species is allowed to change by flipping the spins of lattice sites [43]. In the current calculations, equilibrium is reached once the standard deviation in averaged concentration ($q = 2x - 1$, where x is the molar fraction of solute) in semigrand canonical MC is less than 10^{-4} or that of the energy in canonical MC is less than 0.1 meV/atom. After equilibration, the microstates sampling the low energy region of the configurational space are taken to calculate the thermodynamic averages and the free energy is calculated by thermodynamic integration [43]. Treating the discontinuities in thermodynamic quantities as possible phase transformations, the phase diagram can be calculated using the results of MC simulations, by scanning over fixed chemical potential or temperature. All MC simulations and phase boundary calculations are performed by EMC2 and PHB code in ATAT, respectively. Detailed parameters of CE and MC calculations are listed in Table I.

E. Short-range order analysis

To analyze the evolution of short-range order (SRO) at finite temperatures, the Warren-Cowley SRO parameter is adopted and the SRO for four nearest neighboring (NN) shells are calculated. For a binary alloy with fixed composition and

TABLE I. Detailed parameters of the CE and MC calculations for HCP and FCC lattices. The number of structures in the training, maximum number of atoms of structures, number of pair, triplet, and quadruplet clusters, leave-one-out cross-validation score (LOOCV, meV/atom) [35,36], and size of the MC simulation cells (No. of primitive cells).

Lattice	No. training DFT calc.	Max. No. atoms	No. pair	No. triplet	No. quadruplet	LOOCV	MC cell
HCP	228	18	11	15	0	3.1	37 × 37 × 20
FCC	317	16	23	12	16	3.5	39 × 39 × 39

temperature (T), the Warren-Cowley SRO is defined by [44]

$$\alpha_{lmn}(x,T) = 1 - \frac{P^{A(B)}_{lmn}(x,T)}{x}, \tag{9}$$

where x is the nominal molar fraction of B and $P^{A(B)}_{lmn}(x,T)$ is the conditional probability that given an A atom at the origin, there is a B atom at shell (lmn). If $\alpha_{lmn} > 0$, then A-A pairs are preferred at shell (lmn) since $P^{A(B)}_{lmn}(x,T) < x$, leading to clustering tendency; conversely, $\alpha_{lmn} < 0$ or $P^{A(B)}_{lmn}(x,T) > x$ indicates that A-B pairs are preferred and results in ordering tendency. If the atoms are randomly distributed, then $P^{A(B)}_{lmn}(x,T) = x$ and $\alpha_{lmn} = 0$, leading to solid solution phase without SRO. In the context of generalized Ising model, the Warren-Cowley SRO can also be defined by [45]

$$\alpha_{lmn}(x) = \frac{\langle \bar{\Pi}_{lmn} \rangle - q^2}{1 - q^2}, \tag{10}$$

where $\langle \bar{\Pi}_{lmn} \rangle$ is the averaged correlation for pair clusters at shell (lmn) [see Eq. (5)], and q ($= 2x - 1$) is the concentration in generalized Ising model with $q = -1$ and $q = 1$ referring to pure A and pure B, respectively. For the structures from canonical MC simulations, Eq. (10) is adopted to calculate the SRO of four NN shells as a function of temperature.

III. GROUND-STATE STRUCTURES AND STABILITY

In the CE calculations, the relaxed structures from DFT calculations are examined via the lattice distortion [Eq. (6)] and NMSD to determine whether the structures should be included in the fitting of ECIs. In Figs. 1 and 2, the lattice distortion and NMSD as a function of x_{Sn} and their distributions are shown for relaxation of HCP and FCC orderings. Generally, both the lattice distortion and NMSD become larger as x_{Sn} increases from zero, then decreases as x_{Sn} approaches unit. In the middle region, the lattice distortion and NMSD are significantly larger because the alloy prefers to stay in the lattice of the stable intermetallic compound $\mathrm{Mg_2Sn}$, thus deviating from ideal lattices. Comparatively, the lattice distortion of HCP is generally larger than that of FCC, since the c/a ratio of HCP Mg and Sn are different and while FCC, by definition, always remains cubic. For both HCP and FCC, the lattice distortion drops around 0.1 while NMSD drops at 1%. For consistency, the lattice distortion criterion is chosen to select relaxed structures for the training of ECIs and those with distortion larger than 0.1 is excluded, which is recommended in ATAT [37].

In the current work, the CEs are performed in two steps; first, converged CEs are obtained and all structures with up to 14 and 12 atoms are searched for ground states for HCP and FCC, respectively; then, all the structures with up to 18 and 16 atoms and with $x_{\mathrm{Sn}} \leqslant 25$ at.% are searched using the energies predicted by previously converged CE and those with energies less than 5 meV/atom above the corresponding convex hull are calculated by DFT and further included in the training of the final converged CE. The ECI energies and CE results for HCP and FCC are shown, respectively, in Figs. 3 and 4, where the energies input from DFT, the corresponding energies from CE fitting, the metastable and global convex hulls of formation energy are plotted, with the

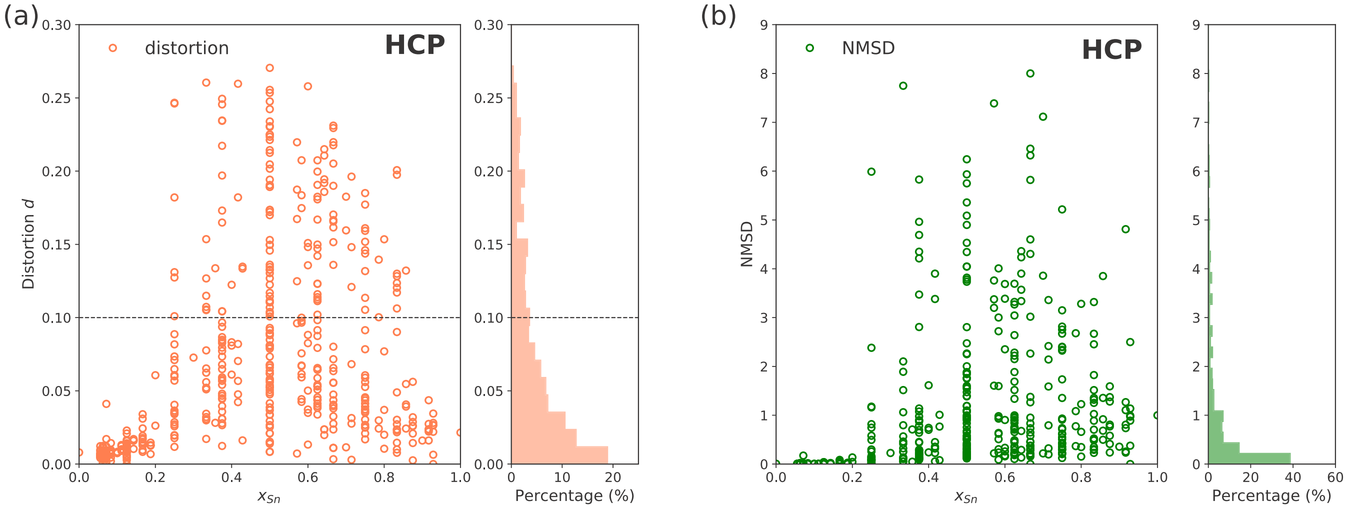

FIG. 1. Relaxation of orderings on HCP lattice as a function of the molar fraction of Sn (left) and its histogram (right) evaluated by the lattice distortion (a) and normalized mean square displacement (b).

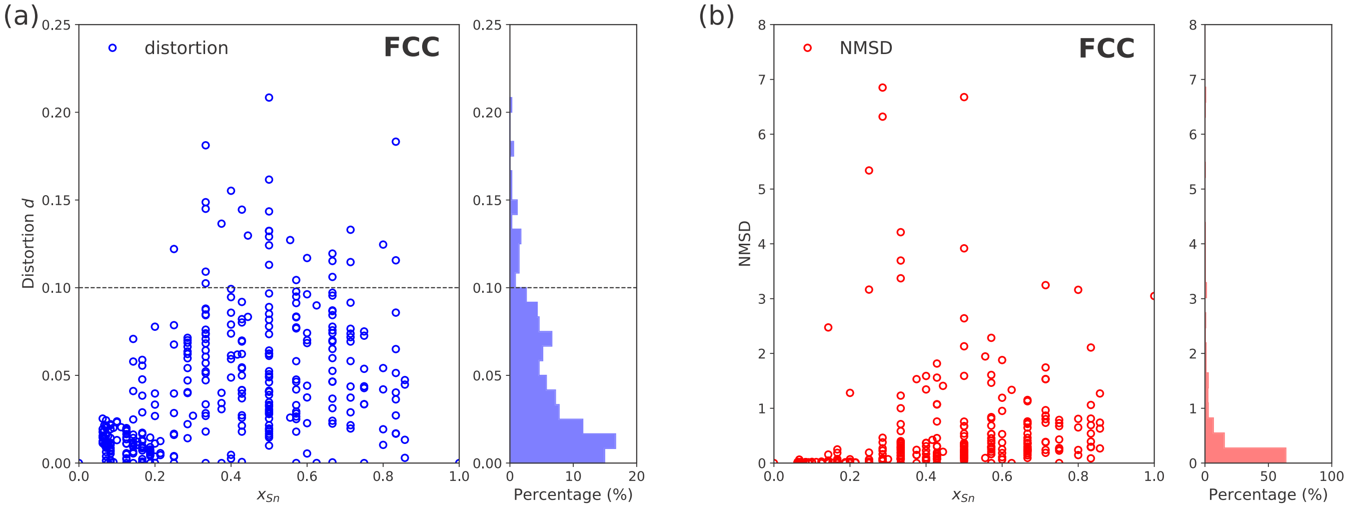

FIG. 2. Relaxation of orderings on FCC lattice as a function of the molar fraction of Sn (left) and its histogram (right) evaluated by the lattice distortion (a) and normalized mean square displacement (b).

energies of HCP Mg and body-centered tetragonal (BCT) Sn as references. Note that α Sn (face-centered diamond), i.e., the ground-state structure of Sn, is not chosen as energy reference, since α Sn is only stable below 298 K [4], while we aim to study the precipitation at high temperatures. The pair and triplet clusters are enough to depict the energies of orderings on HCP lattice [Fig. 3(a)], while quadruplet clusters also contribute to the energies of FCC lattice [Fig. 4(a)]. In both cases, the magnitude of the ECI energy decreases with increasing size of clusters (i.e., largest two-site distance within the cluster). The cutoff distance for pair and triplet interactions for CE of HCP lattice are 7.82 and 5.54 Å, respectively; while that for the pair, triplet and quadruplet interactions for CE of FCC lattice are 13.92, 6.39 and 5.53, respectively. As shown in the convex hulls of formation energies [Figs. 3(b) and 4(b)], $D0_{19}$ Mg_3Sn, B19 MgSn, and $D0_{19}$ $MgSn_3$ are predicted to be on the HCP convex hull, while $L1_2$ Mg_3Sn and $L1_0$ MgSn are on the FCC convex hull. In agreement with previous experimental results, the $D0_{19}$ and $L1_2$ Mg_3Sn phases are identified on the metastable convex hull with energies 32 and 7 meV/atom above the global convex hull, respectively, which indicates that $L1_2$ is more stable than $D0_{19}$ Mg_3Sn. The relative stability of $L1_2$ and $D0_{19}$ Mg_3Sn explains the fact that $L1_2$ Mg_3Sn can be readily formed in aged samples while formation of $D0_{19}$ Mg_3Sn requires increased cooling rate or lowered aging temperatures [17,19,20].

The ordering phases on or slightly above (within 5 meV/atom) the HCP metastable convex hull are shown in Fig. 5, where the primitive cells are indicated by the dashed red lines. Besides $D0_{19}$ [Fig. 5(a)] and B19 [Fig 5(b)], which are on the HCP convex hull, the Sn concentration follows $x_{\mathrm{Sn}} < 25$ at.% for the other orderings. Viewed along the [0001] axis, the $D0_{19}$ phase is made of the switching layers of pure Mg and zigzagged arrangements of Mg / Sn rods on

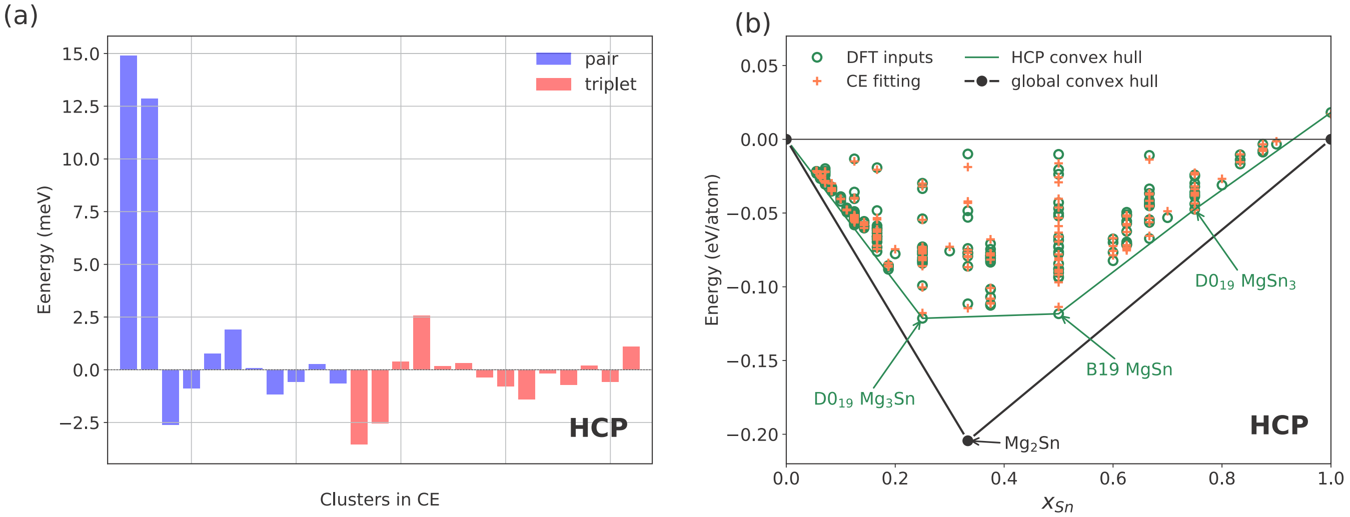

FIG. 3. (a) Effective cluster interaction energies of the clusters in CE for HCP Mg-Sn lattice, where the clusters are ordered with increasing size (largest two-site distance) within the cluster. (b) Formation energies of orderings on the HCP lattice from DFT calculations and cluster expansion (CE). The metastable HCP convex hull and global convex hull are also shown. The structures on the HCP convex hull are labeled.

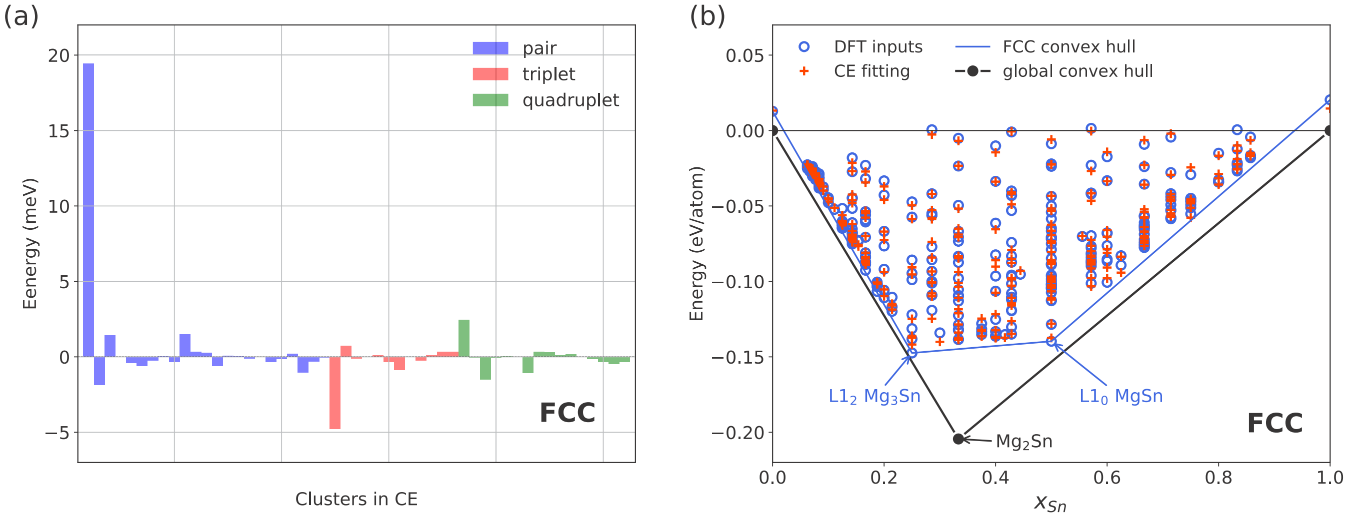

FIG. 4. (a) Effective cluster interaction energies of the clusters in CE for FCC lattice, where the clusters are ordered with increasing size (largest two-site distance) within the cluster. (b) Formation energies of orderings on the FCC lattice from DFT calculations and cluster expansion (CE). The metastable FCC convex hull and global convex hull are also shown. The structures on the FCC convex hull are labeled.

$(01\bar{1}0)$ plane while B19 phase is made of switching layers of pure Mg and Sn on $(01\bar{1}0)$ plane. For all the other orderings with energy slightly above the convex hull between pure Mg and D0$_{19}$, various patterns of atomic arrangements are identified. The most popular arrangements of Sn atoms are indicated by the blue lines in Figs. 5(a), 5(c), and 5(d). Note that these zigzagged arrangements of Sn rods are the basic building blocks of the D0$_{19}$ phase, where such arrangements are stacked compactly with pure Mg. The popularity of such building block is reasonable from a thermodynamic perspective, considering that it is the basic unit of D0$_{19}$ on the HCP convex hull and more layers of pure Mg are present between the zigzagged arrangements of Sn rods for orderings with $x_{\mathrm{Sn}} < 25$ at.% to maintain the overall concentration. Previous studies also revealed such zigzagged patterns of solute rods in Mg-based rare earth alloys, such as Mg-Nd [39] and Mg-Sc systems [46], where, similar to the current results, D0$_{19}$ structure with 25 at.% solute is on the HCP convex hull of formation energies. Apart from such zigzagged building block, other types of arrangements, although less frequently observed, are also identified, such as two-atom rods of Sn

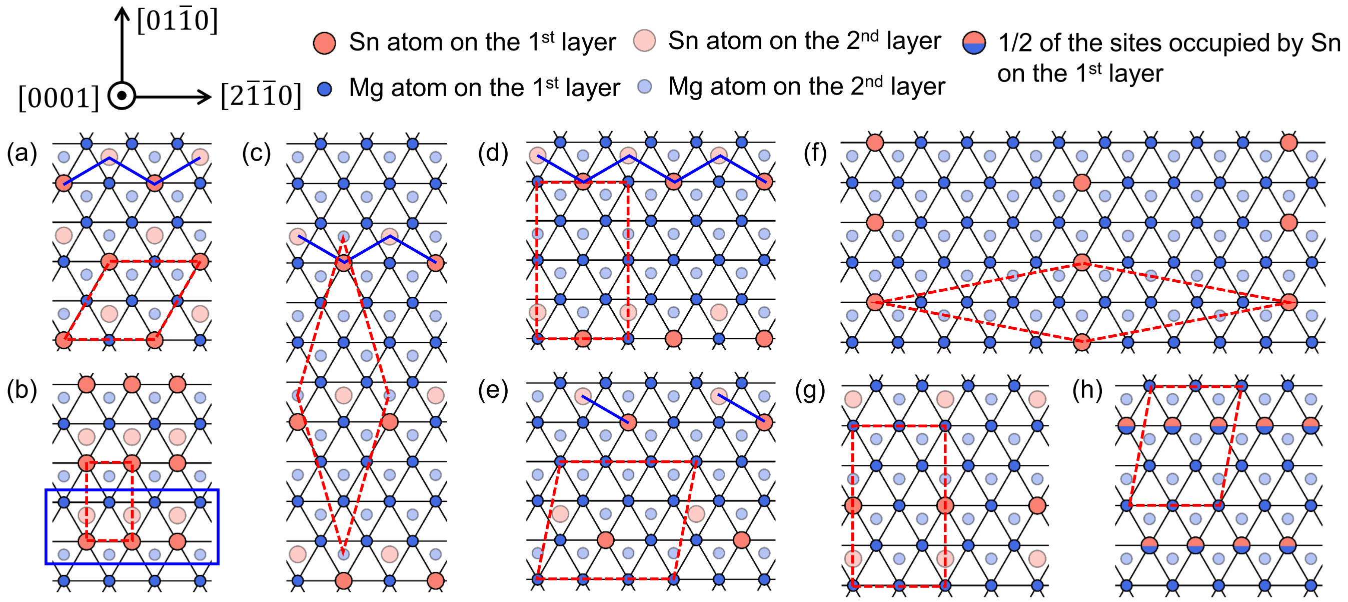

FIG. 5. Schematic crystal structures of orderings on or with energies less than 5 meV/atom above the metastable HCP convex hull. Orderings are shown as viewed along the [0001] axis. The symbols for the atoms are shown in the figure. The triangular basal layers are stacked with an "…ABAB…" sequence when viewed along this axis. The dashed red lines indicate the primitive cell for the ordering phases; the blue lines connect the Sn atoms for the most common building block of the orderings with $x_{\mathrm{Sn}} < 25$ at.%. The structure files shown in this figure in VASP format can be downloaded in the Supplemental Material [55].

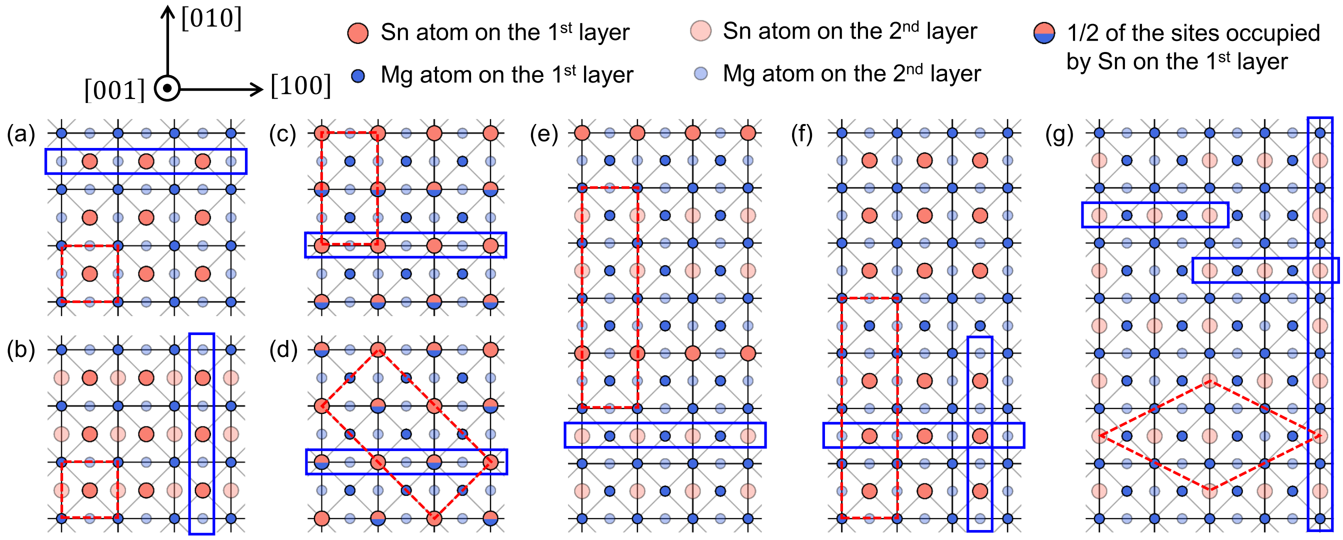

FIG. 6. Schematic crystal structures of orderings on or with energies less than 5 meV/atom above the metastable FCC convex hull. Orderings are shown as viewed along the [001] axis. Relative to this zone axis, the crystal structure can be viewed as a stacking of two centered square lattices. The dashed red rectangles are for the primitive cells of ordering phases; the most common building block for orderings with $x_{\mathrm{Sn}} < 25$ at.% is indicated by blue rectangles. The structure files shown in this figure in VASP format can be downloaded in the Supplemental Material [55].

[Fig. 5(e)], single-atom rods of Sn [Figs. 5(f) and 5(g)], planar arrangements of switching Sn and Mg atoms [Fig. 5(h)].

The ordering phases on FCC lattice with low energies are also studied to reveal the preferred pattern of atomic arrangements. Apart from $L1_2$ [Fig. 6(a)] and $L1_0$ [Fig. 6(b)], other ordering phases with $x_{\mathrm{Sn}} < 25$ at.% and slightly above (within 5 meV/atom) the FCC metastable convex hull are shown [Figs. 6(c) to 6(g)]. Viewed along the [001] direction, the atomic arrangements are examined, where the switching rods of Mg and Sn are found to prevail in these ordering phases (as indicated by blue rectangles), thus becoming the building block for ordering phases on FCC lattice. As shown in Fig. 6, most ordering phases, including $L1_2$ and $L1_0$, can be formed by different arrangements of such building block and pure Mg. Note that circles colored half in blue and half in red indicate that one in every two sites is occupied by Sn atoms along the [001] direction, which can also be categorized as such building blocks. Similar to the case of HCP, the prevalence of such building block can be readily explained thermodynamically, since the stacking of such building block and pure Mg leads to the $L1_2$ and $L1_0$ phases, which are on the FCC convex hull, hence it is energetically favored. We will show, in Sec. VI, that such building blocks in HCP and FCC lattice play a fundamental role in the formation of coherent precipitates at early stages of precipitation.

IV. FINITE-TEMPERATURE STABILITY AND PHASE DIAGRAM

The finite-temperature stability of the phases on the metastable HCP and FCC convex hull and their corresponding phase diagrams are constructed by the semigrand canonical MC simulations, where the total number of lattice sites are fixed and spins for atoms are flipped under constant chemical potential, to search for the state that minimizes the Hamiltonian [43]. To show the principle for phase diagram calculations, the results of MC scans over temperatures and chemical potentials are shown in Figs. 7 and 8. At constant temperatures, the MC simulations yield the convex hull of free energies, where the straight lines connecting the neighboring phases are the common tangent for two-phase equilibria. As temperature increases, the single-phase regions become wider and the convex hull become smoother, approaching the energy curve for the corresponding solid solution phase at high temperatures. For all the temperatures investigated, the free energy of HCP is lower than that of FCC if $x_{\mathrm{Sn}} < 10$

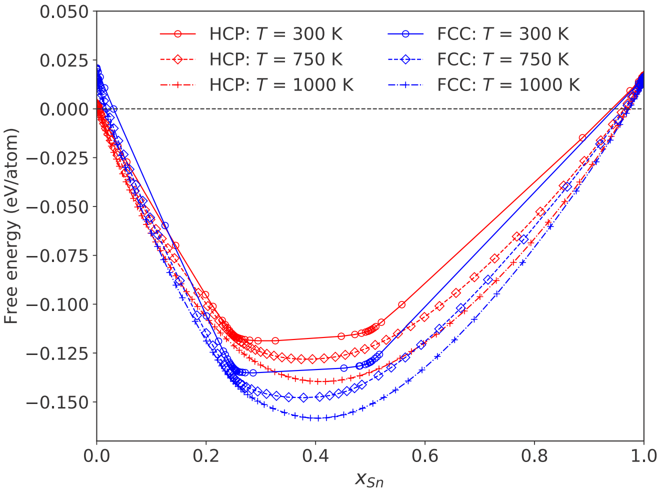

FIG. 7. Free energy convex hull as a function of the molar fraction of Sn at finite temperatures from the semigrand canonical MC simulations for HCP and FCC lattices with the red line and blue line, respectively. Note that the MC simulations directly yields the energy convex hull, not the energy of each phases.

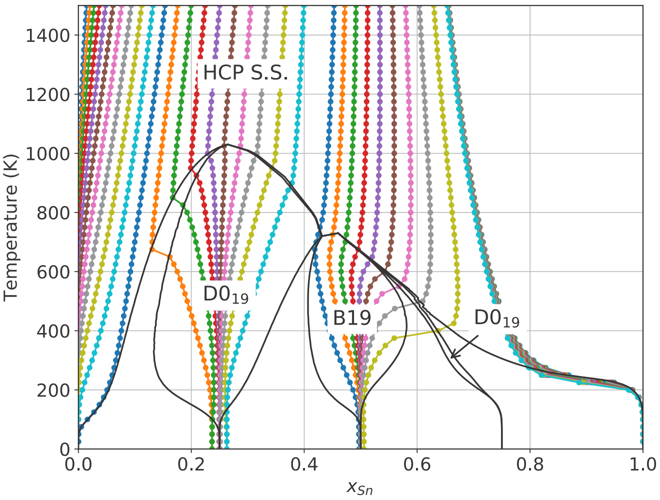

FIG. 8. Illustration of the phase diagram calculations from the MC simulations for HCP lattice. Note that the results of molar fraction of Sn vs. temperature naturally reveals the pattern of the phase diagrams of orderings on HCP lattice.

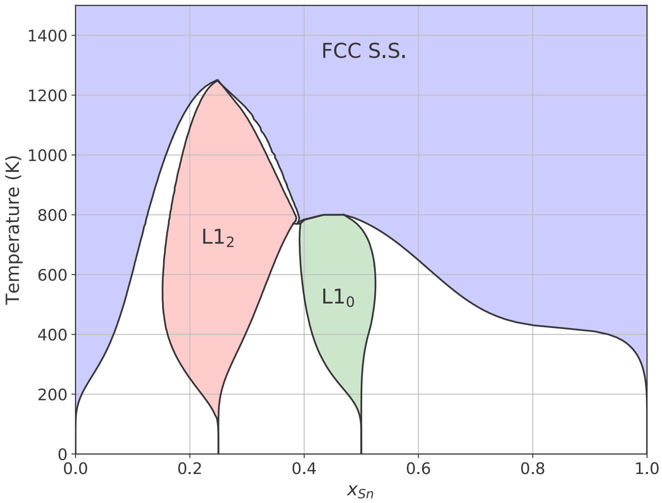

FIG. 10. Phase diagram of the metastable orderings on the FCC convex hull with energies from semigrand canonical MC simulations using CE Hamiltonian.

at.% approximately, while FCC is more stable for $x_{\mathrm{Sn}} > 10$ at.%. Moreover, the MC scans were performed with constant chemical potentials that stabilize different ground states. Using the results of HCP lattice for illustration, the evolution of x_{Sn} as a function of temperature is plotted in Fig. 8, which perfectly reveals the pattern of the underlying HCP phase diagram. As can be seen in Fig. 8, the sudden changes (or discontinuities) in the $x_{\mathrm{Sn}}(T)$ indicates phase transformations, which justifies the use of discontinuities to detect the phase boundaries. It is worth mentioning that, despite the numerical uncertainty, all $x_{\mathrm{Sn}}(T)$ converges to one of the ground-state phases at 0 K, indicating zero configurational entropy at 0 K since no uncertainty of occupancy is allowed.

The boundaries for the ground-state phases and solid solutions, determined by detecting the discontinuities of thermodynamic quantities from MC simulations, are shown in Figs. 9–11, where the single phase regions are colored. On HCP lattice, the stable regions of D0$_{19}$ Mg$_3$Sn, B19 MgSn, and D0$_{19}$ MgSn$_3$, along with HCP solid solutions, are revealed. Note that when the two-phase regions are very narrow, it is difficult to determine the nature of the reaction (e.g., $T = 720$ K and $x_{\mathrm{Sn}} = 45$ at.%) from MC simulations, since the results of MC are innately affected by the randomness and much larger simulation cells are needed to improve the accuracy. The region for D0$_{19}$ MgSn$_3$ is very narrow and agrees with the ground-state convex hull of orderings on HCP lattice, where the energy of D0$_{19}$ MgSn$_3$ is almost on the straight line connecting B19 and HCP Sn (1 meV/atom difference). For orderings on FCC lattice, the diagram of L1$_2$ Mg$_3$Sn, L1$_0$ MgSn and solid solution phase are shown in Fig. 10, where a eutectoid reaction (i.e., FCC solid solution $\rightarrow$ L1$_2$ Mg$_3$Sn + L1$_0$ MgSn) is detected. In both cases of HCP and FCC, the orderings at $x_{\mathrm{Sn}} = 25$ at.% (D0$_{19}$ and L1$_2$)

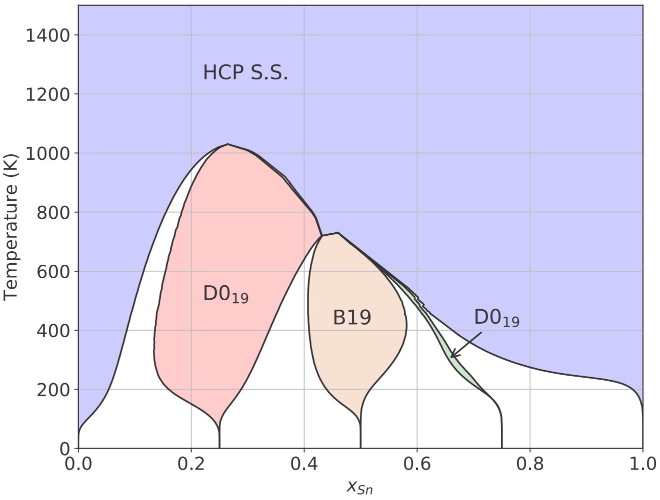

FIG. 9. Phase diagram of the metastable orderings on the HCP convex hull with free energies from semigrand canonical MC simulations using CE Hamiltonian.

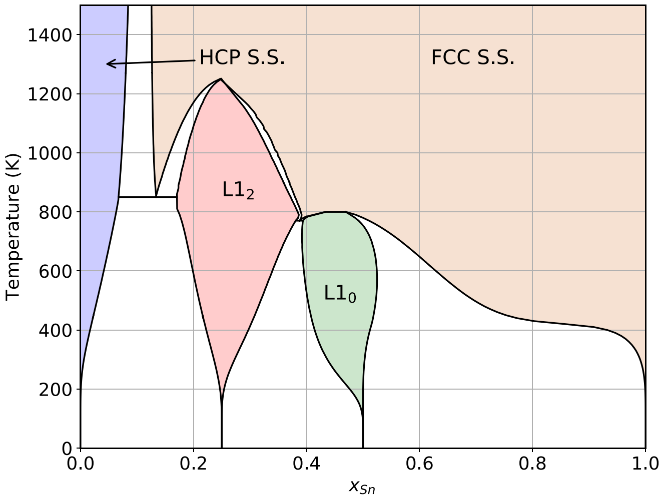

FIG. 11. Phase diagram of the metastable orderings on both HCP and FCC lattices.

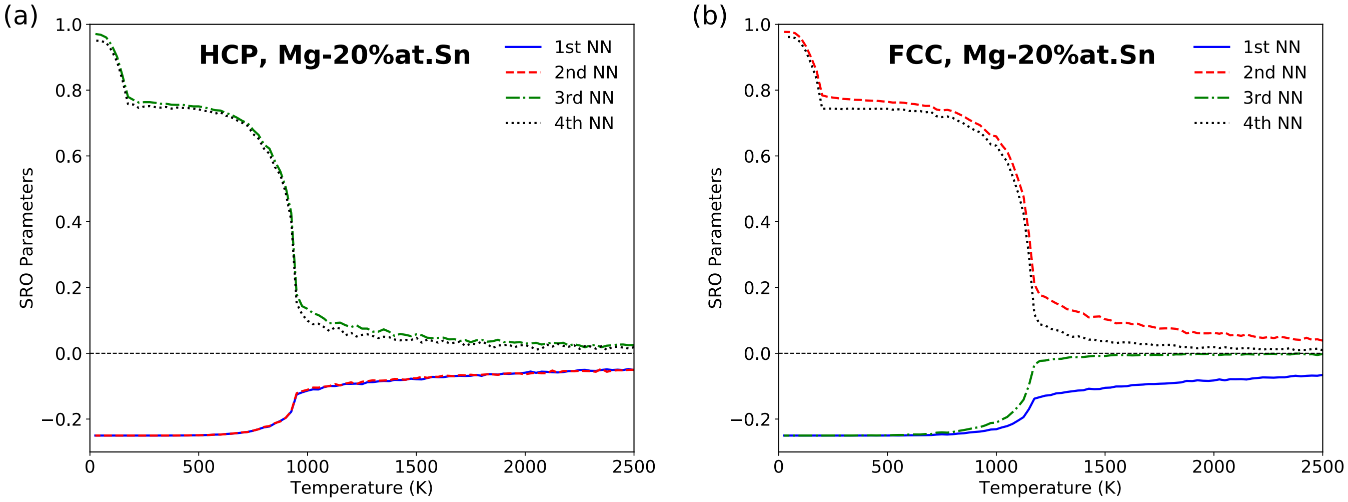

FIG. 12. Warren-Cowley short-range order parameters as a function of temperature for HCP (a) and FCC (b) Mg-20Sn (at.%) from the structures of canonical MC simulations. The results for the first four nearest-neighboring shells are shown.

are more stable than the ones at $x_{\mathrm{Sn}} = 50$ at.% (B19 and $L1_0$) with respect to temperature increase. Using the same reference for energy (i.e., HCP Mg and BCT Sn), the phase diagram orderings on both HCP and FCC is plotted together in Fig. 11. As expected from the free energy convex hulls (Fig. 7), the HCP solid solution remains stable under all the temperatures investigated for $x_{\mathrm{Sn}} \sim< 10$ at.% and the orderings on the FCC lattice are stable at regions of larger x_{Sn}. At $T = 850$ K and $x_{\mathrm{Sn}} = 13$ at.%, an eutectoid reaction (i.e., FCC solid solution $\rightarrow$ HCP solid solution + $L1_2$ Mg_3Sn) is revealed. It should be noted that, the calculated phase boundaries and reactions are only approximate, due to the innate error in DFT energies and neglected effects such as thermal electronic contribution, thermal expansion and anharmonic vibrations [47]. However, the topology of phase diagrams and the nature of the reactions from the calculations of coupled CE and MC with DFT energy input are expected to be reliable [39,46]. Note that, in the phase diagrams from Monte Carlo simulations, some of the phase boundaries are not smooth, which is due to the randomness in MC method. Such non-smooth feature in phase diagrams is not expected in reality due to the fact that the macro-states of the material system are the statistical averages over a large number of subsystems on microscale while, in MC simulations at atomic scale (54760 and 59319 atoms for the case of HCP and FCC, respectively), the fluctuations in the results (i.e., energy, concentration, temperature, etc.) due to the randomness are inevitable. Hence the phase diagrams are presented without further modifications.

In the heat treatment of alloys, the ordering/clustering tendency plays an important role at the early stages of precipitation. Short-range order (SRO) parameter is usually used to quantify the ordering/clustering tendency in alloys [44,45]. To analyze the evolution of SRO in the systems, the canonical MC simulations are performed and the Warren-Cowley SRO parameters α for four NN shells of the output structures are analyzed following the definition from Eq. (10). Irrespective of the shells under consideration, there will always be positive SRO parameters, even for perfectly ordered structures (at 0 K), which indicates SRO exists if SRO parameters for some of the shells are significantly smaller than zero. As shown in Fig. 12, SRO parameters for all the shells approach zero up to 2500 K for the current calculations. However, the SRO parameters are not exactly zero at temperatures well above the transition to solid solution, indicating that the atoms in the solid solution phase are not randomly distributed and there always is some degree of SRO at high temperatures. For HCP, the Warren-Cowley SRO parameters for the 1st and 2nd NN are always negative and those for 3rd and 4th stay positive; while for FCC, the SRO parameter for 1st and 3rd NN are negative and those for 2nd and 4th remain positive, indicating the ordering ($\alpha \ < 0$) / clustering ($\alpha \ > 0$) tendencies differ at different shells. In both cases, the 1st NN prefers ordering, meaning that attractive interaction between Mg and Sn atoms is preferred. Additionally, the phase transformations can also be revealed by the sudden change of SRO parameters. As temperature decreases, there will be transformations from solid solution to $D0_{19}$ or $L1_2$ phases, caused by the changing magnitude of SRO parameters for all the shells, although their signs do not change. Further decreasing of temperature leads to the precipitation of pure Mg from the ordered phases ($D0_{19}$ or $L1_2$), which is only caused by magnitude of clustering (not ordering) tendencies.

V. EFFECT OF LATTICE VIBRATIONS ON $L1_2$ MG_3SN STABILITY

As mentioned before, the phase boundaries obtained from the MC simulations with coupled CE and DFT energies are not accurate enough to compare with experiments due to the innate inaccuracy in DFT energies and the neglected effects. One of neglected effects is the free energy due to lattice vibrations. Previous first-principles calculations [48] and molecular dynamics simulations with angular dependent potential [49] for θ' and θ Al_2Cu show that θ' is stable at low temperatures while θ is stabilized by vibrational entropy as temperature increases. This indicates that the effect of lattice vibrations can play an important role in stabilizing competitive phases when their enthalpies of formation are close to each other. In the current work, the effect of vibrational free energy on the stability of phases at $x_{\mathrm{Sn}} = 25$ at.%, i.e., $D0_{19}$ Mg_3Sn, $L1_2$

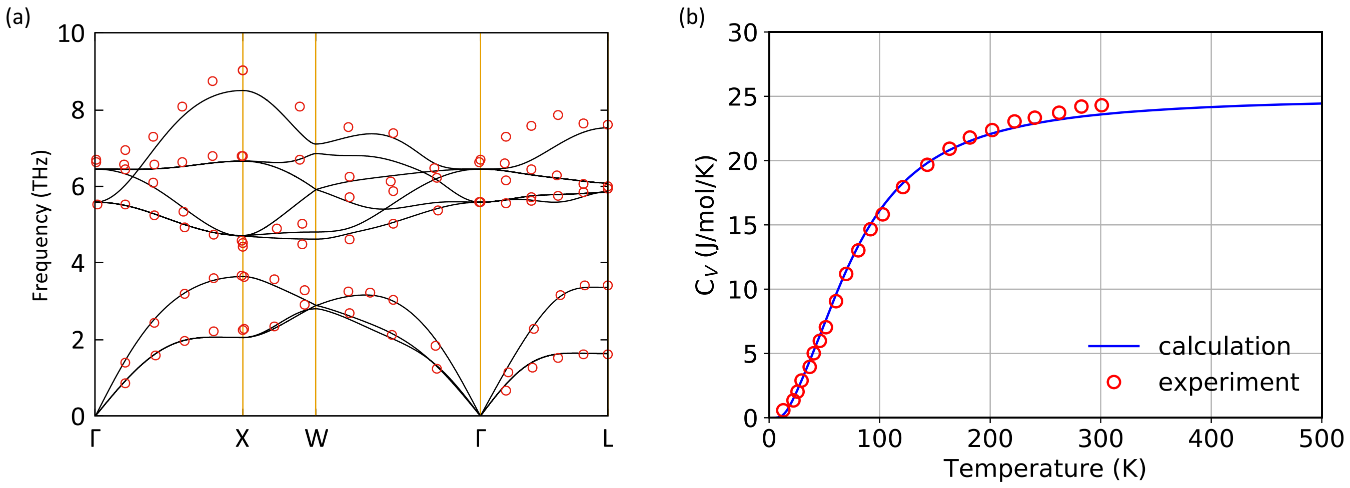

FIG. 13. The phonon dispersion relation and heat capacity from linear response method. Note that the experimental dispersion relation of Kearney *et al.* [50] and the heat capacity of Jelinek *et al.* [52] are adopted to validate the calculations.

Mg_3Sn and mixture of pure Mg and β Mg_2Sn, are analyzed with the phonon density of states determined by the force constant matrix calculated by the linear response method [30] with harmonic approximation. To test the accuracy of harmonic phonon calculations, the calculated phonon dispersion relation and the heat capacity (C_V) of Mg_2Sn are compared to the experiments. As shown in Fig. 13(a), the calculated phonon dispersion relation generally agrees well with the experiment of Kearney *et al.* [50], except for some disagreement at high-frequency branches. In principle, the low frequency phonon modes (hence low energy) will contribute much more to the thermodynamics according to Boltzmann statistics [51], and disagreement in the high-frequency branch is expected to affect the thermodynamics insignificantly. The calculated C_V agrees well with experiments up to 300K, where the experimental data is available [52]. Therefore, the methods and parameters in harmonic phonon calculations are expected to be reliable.

The free energies consisting of ground-state static energy and vibrational free energy for Mg, Mg_2Sn, $D0_{19}$, and $L1_2$ Mg_3Sn, are shown in Fig. 14. The mixture of Mg and Mg_2Sn with overall 25 at.% Sn, i.e., 25at.% Mg and 75at.% Mg_2Sn, is the most stable at low temperatures and $L1_2$ Mg_3Sn becomes the stable one when $T > 353$ K, while $D0_{19}$ Mg_3Sn always remains metastable. Despite the inaccuracies in the transition temperature, it is clearly shown that $L1_2$ structure becomes stable at high temperatures due to vibrational free energy. This is similar to the case of the competition between θ' and θ Al_2Cu [48,49] and suggests the $L1_2$ Mg_3Sn phase may be included in the equilibrium phase diagram for Mg-Sn alloys at finite temperature.

VI. EARLY STAGES OF PRECIPITATION

In the microstructures of Mg-9.8Sn (wt.%) alloy aged at $100 \sim 250\,^{\circ}$C, G.P. zone and $L1_2$ Mg_3Sn on the basal plane of HCP matrix are observed [17,18]. And the $D0_{19}$ Mg_3Sn phase on the basal plane are also observed in the as-solidified microstructure with increased cooling rate or lowered aging temperature [19,20]. Previously, the precipitation sequence of supersaturated solid solution → G.P. zone → $L1_2$ Mg_3Sn → βMg_2Sn is proposed in accordance with the experimental observations [17]. However, the role of $D0_{19}$ Mg_3Sn and detailed steps of how G.P. zone transforms to β Mg_2Sn are not discussed.

In the current work, many ordering phases close to the HCP and FCC convex hulls (within 5 meV/atom) are predicted, in addition to the phases on the metastable convex hulls. In the following, the roles of these ordering phases in the early stages of precipitation are analyzed. Among the many ordering phases on the HCP lattice, several have layered Sn atoms on the basal plane of HCP matrix, although the layers are only partially occupied by Sn atoms. One of the orderings

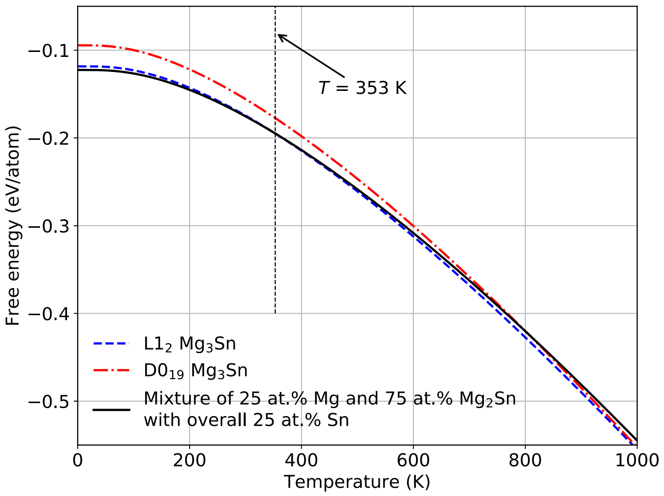

FIG. 14. Free energies with contributions from ground-state static energy and vibrational free energy of Mg-25Sn (at.%) alloy in $D0_{19}$ structure, $L1_2$ structure and as a mixture of Mg and Mg_2Sn with overall 25 at.% Sn (i.e., 25at.% Mg and 75at.% Mg_2Sn). It is shown that the $L1_2$ and $D0_{19}$ can be stabilized by vibrational entropy and $L1_2$ becomes the stable phase at high temperatures. The dashed line indicates the transition temperature between $L1_2$ Mg_3Sn and β Mg_2Sn.

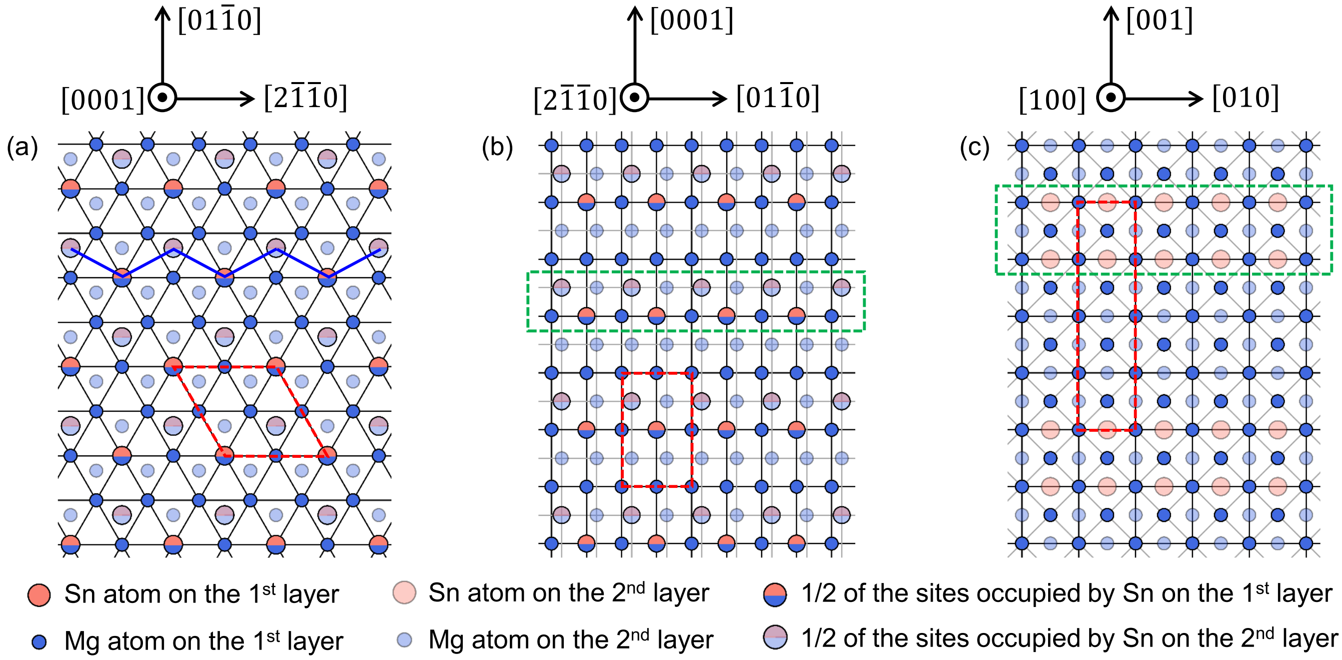

FIG. 15. Orderings on HCP and FCC lattice predicted by the current CEs that are likely to be related to the early stages of precipitation. Potential G.P. zone on HCP lattice viewed along [0001] (a) and [2$\bar{1}\bar{1}$0] direction (b); (c) potential G.P. zone on FCC lattice (viewed along [001]) where the layered region resembles $L1_2$ symmetry. The red dashed lines indicate the primitive cell for the ordering phase; the blue lines in (a) indicate the arrangement of Sn atoms that resembles the most common building block of orderings on HCP lattice; the green dashed rectangles indicate the regions on the HCP and FCC G.P. zones in (b) and (c) that resemble $D0_{19}$ and $L1_2$ Mg_3Sn, respectively. The structure files shown in this figure in VASP format can be downloaded in the Supplemental Material [55].

with a nominal composition of 12.5 at.% Sn is viewed along [0001] and [2$\bar{1}\bar{1}$0] and shown in Figs. 15(a) and 15(b). The Sn atoms are aligned in a zigzagged fashion on the basal plane [blue lines in Fig. 15(a)], with a layer spacing equal to lattice parameter along c axis of HCP Mg. Viewed along both [0001] and [2$\bar{1}\bar{1}$0] directions, half of some lattice sites are occupied by Sn atoms. Compared with the $D0_{19}$ Mg_3Sn structure, it is obvious that this ordering is exactly one layer of $D0_{19}$ Mg_3Sn [dashed green rectangles in Fig. 15(b)] and one layer of pure Mg stacked repeatedly, with the thickness of each layer being the lattice parameter along c axis of HCP matrix. Although the alloys in experiments have a smaller x_{Sn} (i.e., 9.8 wt.% is equivalent to 2.2 at.% [17]), the solute atoms will segregate at the solid / liquid interface in the solidification process and diffusion of Sn atoms will also occur at high-temperature solutioning treatment, leading to Sn enriched regions. Thus, the coherent ordering in Figs. 15(a) and 15(b) is a potential G.P. zone in Mg-Sn alloys, which is likely to be the precursor for the formation of $D0_{19}$ Mg_3Sn phase in Mg matrix. Furthermore, it is well known that the close-packed planes of HCP and FCC are stacked in "$\cdots ABABAB \cdots$" and "$\cdots ABCABC \cdots$" fashion, respectively, and that the stacking fault region in HCP lattice resembles FCC structure [18]. Considering that $D0_{19}$ and $L1_2$ Mg_3Sn have the same stoichiometry, it is very likely layers of $L1_2$ Mg_3Sn are formed by the advent of stacking fault in HCP matrix with $D0_{19}$ ordering [17] and then rearrangement of Sn atoms without long distance diffusion (larger than a few lattice parameters), resulting in layers of $L1_2$ Mg_3Sn embedded in the FCC parent lattice of Mg; see the green dashed rectangles in Fig. 15(c). Eventually, the transformation from $L1_2$ Mg_3Sn to β Mg_2Sn, both of which have FCC symmetry, can readily proceed on the basal plane of HCP matrix, by the further enrichment and rearrangement of Sn atoms. So far, the physical picture of the precipitation sequence, i.e., supersaturated solid solution → G.P. zone → $D0_{19}$ Mg_3Sn → $L1_2$ Mg_3Sn → βMg_2Sn, is complete. Note that the current proposed sequence also explains why the $L1_2$ Mg_3Sn and β Mg_2Sn plates are aligned on the basal plane of HCP matrix [17]. Recently, Wang *et al.* [53] proposed a method to obtain the precipitation sequence based on the monotonic decrease of the formation energy per solute atom, which shows good agreement with experiments. Note that our proposed precipitation sequence exactly follows the energy decrease criterion of Wang *et al.* [53]. The spacing between the Sn-rich layers in experiments might be different from Fig. 15, due to the fact that x_{Sn} of alloys in experiment is usually much smaller (∼2 at.%) than the overall concentration of those orderings in Fig. 15, i.e., $x_{\mathrm{Sn}} = 12.5$ at.%. Another effect that might contribute to spacing of Sn rich layers is the constitutive strain energy [54], which is not incorporated in the current real-space CE, since CSE can be long-ranged while real-space CE only accounts for short-range interactions [34].

VII. CONCLUSIONS

In the current work, first-principles DFT calculations, CE and MC, are adopted to study the ground-state and finite-temperature structures and stability of the orderings on HCP and FCC Mg-Sn alloys, and the indications on the early stages of precipitation are discussed. Coupling CE and DFT, it is found that $D0_{19}$ Mg_3Sn, B19 MgSn and $D0_{19}$ $MgSn_3$ are predicted to be on the HCP convex hull while $L1_2$ Mg_3Sn and $L1_0$ MgSn are on the FCC convex hull. Particularly, $L1_2$ Mg_3Sn and $D0_{19}$ Mg_3Sn are 7 meV/atom and 32 meV/atom above the global convex hull, indicating that $L1_2$ Mg_3Sn can be more easily observed, in agreement with experiments. Apart from the structures exactly on the metastable convex hulls, many ordering phases, including structures that resemble the G.P. zone in experiments, are predicted to be very close to the corresponding convex hulls. Using the CE Hamiltonian as input for MC simulations, the phase diagrams for the orderings on HCP and FCC lattices are constructed by detecting the discontinuities in the thermodynamic quantities. As expected, $D0_{19}$ and $L1_2$ Mg_3Sn have large stable regions on the HCP and FCC phase diagrams, respectively, while only $L1_2$ Mg_3Sn is stable when phases on both lattices are considered together. Analysis of the effect of lattice vibrations on phase stability indicates that $L1_2$ Mg_3Sn is stabilized by vibrational entropy and become the stable phase at high temperatures. The role of the coherent orderings in the early stages of precipitation is discussed and the precipitation sequence of supersaturated solid solution → G.P. zone → $D0_{19}$ Mg_3Sn → $L1_2$ Mg_3Sn → βMg_2Sn is proposed.

ACKNOWLEDGMENTS

The authors are grateful to the support from the University of Virginia start-up funds. The authors acknowledge Advanced Research Computing Services and IT support at School of Applied Engineering and Sciences at the University of Virginia for providing computational resources and technical support that have contributed to the results reported within this paper.

[1] J. F. Nie, Metall. Mater. Trans. A **43**, 3891 (2012).

[2] M. Esmaily, J. E. Svensson, S. Fajardo, N. Birbilis, G. S. Frankel, S. Virtanen, R. Arrabal, S. Thomas, and L. G. Johansson, Prog. Mater. Sci. **89**, 92 (2017).

[3] A. A. Nayeb-Hashemi and J. B. Clark, Bull. Alloy Phase Diagr. **5**, 466 (1984).

[4] B. C. Zhou, S. L. Shang, Y. Wang, and Z. K. Liu, CALPHAD **46**, 237 (2014).

[5] Y. Zuo and Y. A. Chang, CALPHAD **17**, 161 (1993).

[6] C. F. Glover, T. W. Cain, and J. R. Scully, Corrosion Sci. **149**, 195 (2019).

[7] T. W. Cain, C. F. Glover, and J. R. Scully, Electrochim. Acta **297**, 564 (2019).

[8] X. N. Gu, Y. F. Zheng, Y. Cheng, S. P. Zhong, and T. F. Xi, Biomater. **30**, 484 (2009).

[9] C. Zhao, F. Pan, S. Zhao, H. Pan, K. Song, and A. Tang, Mater. Sci. Eng. C **54**, 245 (2015).

[10] R. Radha and D. Sreekanth, J. Magnesium Alloys **5**, 286 (2017).

[11] S. E. Henderson, K. Verdelis, S. Maiti, S. Pal, W. L. Chung, D. T. Chou, P. N. Kumta, and A. J. Almarza, Acta Biomater. **10**, 2323 (2014).

[12] M. A. Gibson, X. Fang, C. J. Bettles, and C. R. Hutchinson, Scripta Mater. **63**, 899 (2010).

[13] G. Nayyeri and R. Mahmudi, Mater. Sci. Eng. A **527**, 4613 (2010).

[14] A. Zindal, J. Jain, R. Prasad, S. S. Singh, and P. Cizekc, Mater Sci Eng A **706**, 192(2017).

[15] T. T. Sasaki, K. Oh-Ishi, T. Ohkubo, and K. Hono, Scripta Mater. **55**, 251 (2006).

[16] S. Harosh, L. Miller, G. Levi, and M. Bamberger, J. Mater. Sci. **42**, 9983 (2007).

[17] C. Q. Liu, H. W. Chen, H. Liu, X. J. Zhao, and J. F. Nie, Acta Mater. **144**, 590 (2018).

[18] C. Liu, H. Chen, N. Wilson, and J. F. Nie, Scripta Mater. **155**, 89 (2018).

[19] Y. K. Kim, D. H. Kim, W. T. Kim, and D. H. Kim, Mater. Lett. **113**, 50 (2013).

[20] L. Ye, Y. Zhuang, D. Zhao, S. Jia, J. Zhou, J. Gui, and J. Wang, Micron **115**, 1 (2018).

[21] A. van de Walle, JOM **65**, 1523 (2013).

[22] A. Van der Ven, J. C. Thomas, B. Puchala, and A. R. Natarajan, Annual Rev. Mater. Res. **48**, 27 (2018).

[23] A. van De Walle and G. Ceder, Rev. Modern Phys. **74**, 11 (2002).

[24] G. Kresse and D. Joubert, Phys. Rev. B **59**, 1758 (1999).

[25] J. P. Perdew, K. Burke, and M. Ernzerhof, Phys. Rev. Lett. **77**, 3865 (1996).

[26] G. Kresse and J. Furthmüller, Phys. Rev. B **54**, 11169 (1996).

[27] G. Kresse and J. Furthmüller, Comput. Mater. Sci. **6**, 15 (1996).

[28] M. Methfessel and A. T. Paxton, Phys. Rev. B **40**, 3616 (1989).

[29] P. E. Blöchl, O. Jepsen, and O. K. Andersen, Phys. Rev. B **49**, 16223 (1994).

[30] S. Baroni, S. de Gironcoli, A. Dal Corso, and P. Giannozzi, Rev. Mod. Phys. **73**, 515 (2001).

[31] X. H. Liu, Y. Wang, J. O. Sofo, T. J. Zhu, L. Q. Chen, and X. B. Zhao, J. Mater. Res. **30**, 2578 (2015).

[32] Y. Wang, L. Q. Chen, and Z. K. Liu, Comput. Phys. Commun. **185**, 2950 (2014).

[33] J. M. Sanchez, F. Ducastelle, and D. Gratias, Physica A **128**, 334 (1984).

[34] D. B. Laks, L. G. Ferreira, S. Froyen, and A. Zunger, Phys. Rev. B. **46**, 12587 (1992).

[35] A. van de Walle and G. Ceder, J. Phase Equilibria **23**, 348, (2002).

[36] A. van de Walle, M. Asta, and G. Ceder, CALPHAD **26**, 539 (2002).

[37] A. van de Walle, CALPHAD **33**, 266 (2009).

[38] A. H. Nguyen, C. W. Rosenbrock, C. S. Reese, and G. L. Hart, Phys. Rev. B. **96**, 014107 (2017).

[39] A. R. Natarajan, E. L. S. Solomon, B. Puchala, E. A. Marquis, and A. Van der Ven, Acta Mater. **108**, 367 (2016).

[40] R. Sun and A. van de Walle, CALPHAD **53**, 20 (2016).

[41] A. van de Walle, Q. Hong, S. Kadkhodaei, and R. Sun, Nat. Commun. **6**, 7559 (2015).

[42] See CHECKRELAX code of Alloy Theoretic Automated Toolkit (ATAT), https://www.brown.edu/Departments/Engineering/Labs/avdw/atat/.

[43] A. van de Walle and M. Asta, Modelling Simul. Mater. Sci. Eng. **10**, 521, (2002).

[44] J. M. Cowley, Phys. Rev. **77**, 669 (1950).

[45] C. Wolverton, V. Ozolins, and A. Zunger, Phys. Rev. B. **57**, 4332 (1998).

[46] A. R. Natarajan and A. Van der Ven, Phys. Rev. B. **95**, 214107 (2017).

[47] T. Hickel, B. Grabowski, F. Körmann, and J. Neugebauer, J. Phys. Condensed Matter **24**, 053202 (2011).

[48] C. Wolverton and V. Ozolins, Phys. Rev. Lett. **86**, 5518 (2001).

[49] F. Apostol and Y. Mishin, Phys. Rev. B. **83**, 054116 (2011).

[50] R. J. Kearney, T. G. Worlton, and R. E. Schmunk, J. Phy. Chem. Solids **31**, 1085 (1970).

[51] B. Fultz, Prog. Mater. Sci. **55**, 247 (2010).

[52] F. J. Jelinek, W. D. Shickell, and B. C. Gerstein, J. Phys. Chem. Solids **28**, 267 (1967).

[53] D. Wang, M. Amsler, V. I. Hegde, J. E. Saal, A. Issa, B. C. Zhou, X. Zeng, and C. Wolverton, Acta Mater. **158**, 65 (2018).

[54] C. Wolverton, Modelling Simul. Mater. Sci. Eng. **8**, 323 (2000).

[55] See Supplemental Material at http://link.aps.org/supplemental/10.1103/PhysRevMaterials.4.013606 for structure files of Figs. 5, 6, and 15.